

Fizeau Interferometry Testbed: Wavefront Control

Richard G. Lyon

NASA/GSFC Code 935

Greenbelt MD 20771

Ph: 301-286-4302 email: Richard.G.Lyon@nasa.gov

Kenneth G. Carpenter – NASA/GSFC Code 681

Lisa Mazzuca – NASA/GSFC

Hubert Huet, Paul Cottle, Peter Petrone, Peter Dogoda, Peter Liiva, Joe Marzouk
Sigma Research and Engineering, Lanham MD 20706

Gregory Solyar – GEST/UMBC

David Mozurkewich – Seabrook Engineering

NASA/GSFC Code 441 Greenbelt MD 20771

Xiaolei Zhang, Thomas Armstrong – Naval Research Lab, Washington DC 20375

ABSTRACT

Stellar Imager (SI) is a potential NASA space-based UV imaging interferometer to resolve the stellar disks of nearby stars. SI would consist of 20 - 30 separate spacecraft flying in formation at the Earth-Sun L2 libration point. Onboard wavefront control would be required to initially align the formation and maintain alignment during science observations and after array reconfiguration. The Fizeau Interferometry Testbed (FIT) is a testbed currently under development at the NASA/Goddard Space Flight Center to develop and study the wavefront control methodologies for Stellar Imager and other large, sparse aperture telescope systems. FIT consists of 7 articulated spherical mirrors in a Golay pattern, expandable upto 30 elements, and reconfigurable into multiple array patterns. FIT's purpose is to demonstrate image quality versus array configuration and to develop and advance the wavefront control for SI. FIT uses extended scene wavelength, focus and field diversity to estimate the wavefront across the set of apertures. The recovered wavefront is decomposed into the eigenmodes of the control matrix and actuators are moved to minimize the wavefront piston, tip and tilt. Each mirror's actuators are 3 degrees of freedom, however, they do not move each of the mirrors about a point on each mirrors surface, thus the mapping from wavefront piston, tip/tilt to mirror piston, tip/tilt is not diagonal. We initially estimate this mapping but update it as part of wavefront sensing and control process using system identification techniques. We discuss the FIT testbed, wavefront control methodology, and show initial results from FIT.

Keywords: Imaging interferometry, wavefront sensing, optical control, phase retrieval, phase diversity

1. INTRODUCTION

The Fizeau Interferometer Testbed is a ground-based laboratory testbed for the Stellar Imager (SI, <http://hires.gsfc.nasa.gov/~si>) [1], [2]) and other future Sparse Aperture or Fizeau Interferometric systems (e.g., MAXIM and Planet Imager). SI is an UV-optical interferometry mission in NASA's Sun-Earth Connection far-horizon roadmap with a mission time anticipated in the 2015 – 2020 time frame. The primary science goals of SI require both spatial and temporal resolution of stellar magnetic activity patterns in a sample of stars representing a broad range of activity level. The study of these patterns will enable improved forecasting of solar/stellar magnetic activity as well as an improved understanding of the impact of that magnetic activity on planetary climate and astrobiology. SI will also measure internal structure and rotation of these stars using the technique of asteroseismology and determine their relation to the stellar dynamos. The observatory will also image the central stars in external solar systems and enable an assessment of the impact of stellar activity on the habitability of the planets in those systems, thus complementing the assessment of external solar systems that will be done by the planet finding and

imaging missions, such as the Space Interferometer Mission (SIM), Terrestrial Planet Finder (TPF) and Planet Imager (PI).

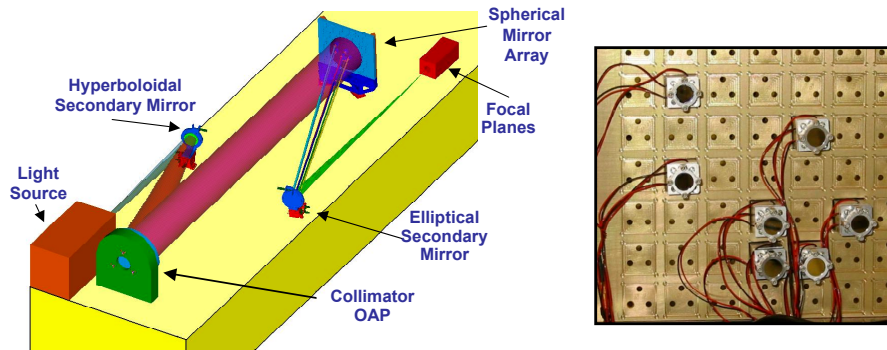


Figure 1
Left: Optical Layout of FIT, Right: Sparse Aperture Array Plate

The mission calls for a reconfigurable array of 10-30 one-meter class spherical mirrors to be used in a Fizeau, or image plane beam combination mode. The maximum baseline length is ~ 500 meters. The wavelength range of operation will be in the optical for asteroseismology and in the ultraviolet for surface imaging, including two of the important emission lines for studying the stellar dynamo behavior, i.e. the chromospheric Mg II h&k lines near 2800 Angstroms and the transition region C IV doublet at 1550 Angstroms. The best angular resolution achievable is ~ 60 micro-arcsec at 1550 Angstroms, which corresponds to about 40,000 km linear resolution for a sun-like star at a distance of 4 parsec. There will be approximately 33 1D linear resolution elements at the equator of a typical nearby dwarf star, and approximately 1000 2D resolution elements to cover the stellar surface. The spectroscopic capability include passbands as narrow as a few Angstroms up to hundreds of Angstroms, from the UV up into the optical wavelengths. It is intended to be a long-term (~ 10 year) mission to permit the study of stellar magnetic activity and cycles.

During the initial conception phase of SI, both the Michelson (pupil plane beam combination) and the Fizeau (image plane beam combination) modes have been considered. The Fizeau configuration was chosen in the end because of several advantages it offered for a mission like SI. Since the Michelson approach requires that the beams from all of the elements be combined and interfered pairwise with each of the other beams, the total number of elements is limited to 10 or less in order to avoid overly complicated beam combiner designs. The Michelson option thus requires numerous reconfigurations of the array to obtain full baseline coverage. The Fizeau approach, on the other hand, could possibly utilize a much larger number (~ 30) of simpler and less expensive one-meter class flat or spherical mirrors on microsats, distributed on a spherical or paraboloidal surface. The light beams from all the elements would be combined simultaneously on one detector, although they could be picked up and combined in subsets if desired. This option requires far fewer reconfigurations (i.e. 2 instead of 20) to obtain a synthesized image, which should save both time and propellant. This option should also utilize fewer reflections, an important consideration if the facility is to operate in the ultraviolet.

Despite the recent surge of development effort in both ground-based as well as space-based interferometry, motivated in part by the needs of the various planet finding and imaging missions, most of the effort has so far been focused on the development of the Michelson type of interferometers, with comparatively little effort for the Fizeau type. This disparity is partly due to the myth that "if Michelson interferometry is hard, Fizeau interferometry is *impossibly* hard". It is true that while Michelson interferometry in general requires only the *knowledge* of the baselines and optical paths to a fraction of the observing wavelength, Fizeau interferometry generally requires the *control* of these same parameters to a fraction of a wavelength, at least in the direct imaging mode. For ground-based applications, this increased accuracy requirement on the control of pathlengths and baselines also translates to a fast and high-accuracy sensing of the wavefront (or optical alignment) in order to derive high bandwidth control signals to combat the fast-changing atmosphere. In the space environment, however, the hope is that most of the environmental changes will be much slower, and wavefront sensing and control loop can thus operate at a much slower speed, which gives

more flexibility on the methods one can adopt to hierarchically phase up all the array elements. Laser metrology of parts of the optics susceptible to internal high frequency mechanical vibrations may be needed to assist in the operations of the main wavefront sensing and control loop.

An added advantage often cited for a Fizeau type of configuration is its wide instantaneous field of view, determined solely by the off-axis optical performance of the system and by the size of the detector. A Michelson type of interferometer potentially can also achieve wide field of view utilizing a large format detector array [3], though long strokes of the delay-lines are needed, and, in the case of small number of mirrors, numerous interferometer reconfigurations as well. (Note: this is not important for the study of single stars, but may be of great interest for the study of mass-exchanging binaries and other, more extended, astrophysical objects.)

In order to gain insight into understanding the requirements, wavefront sensing, control algorithms, post-processing and the error budgeting formalism, for the Stellar Imager mission, a ground testbed, is under developed at NASA/Goddard Space Flight Center. The first phase of this Fizeau Interferometer Testbed contains 7 articulated mirrors but in its final form it will include up to 30 articulated mirrors, commandable automatically by a closed-loop feedback system utilizing extended scene phase diversity to sense the wavefront.

The primary objectives of FIT are:

- Explore the principles of and requirements for the SI mission concept, as well as other Fizeau type interferometers and other sparse aperture telescopes.
- Utilize 7-30 separate apertures, each with 5 degrees of freedom (tip, tilt, piston, as well as 2d translations) in a sparse distribution.
- Demonstrate closed-loop control of articulated mirrors and the overall system to keep beams in phase and optimize imaging.
- Determine the system requirements for accuracy, stability and range of the optics and controls as well as metrology, vibration and stray light. These will be translated into requirements for station keeping and formation-wide metrology for the SI.
- Enable critical assessment of various wavefront sensing algorithms including a variety of phase retrieval and phase diversity approaches; assess image reconstruction algorithms, including CLEAN, MEM, etc. for utility and accuracy by application to real data.
- Investigate optimal sampling methodologies of the Fourier uv-plane, and the optimal implementation of that sampling via time-efficient and propellant efficient reconfigurations of the array.
- Confirm achievable sensitivities for given Fourier uv-plane sampling and coverage; determine the optimal number of collectors, dish size, and formation.

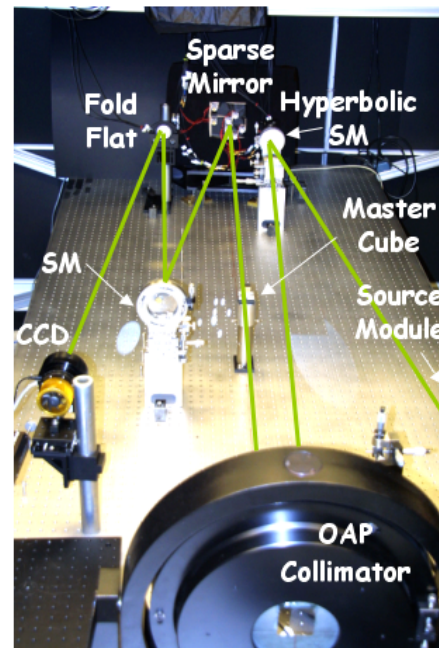


Figure 2 – FIT with baffles removed

In the next sections we describe in more detail the FIT design, including the optical, mechanical, and data acquisition systems, the wavefront sensing and optical control approaches, and show some of the initial results of phasing the array.

2.0 OVERVIEW OF THE FIT SYSTEM

A schematic drawing of the FIT design is given in Figure 1. The initial FIT is designed to operate at optical wavelengths and use a minimum-redundancy array [4] [5] for the primary mirror segments. An extended-

scene film is illuminated by the light from the source assembly. The scene is located in the focal plane of the collimator mirror assembly, which consists of a hyperboloid secondary and an off-axis paraboloid primary. The collimated light is then intercepted by the elements of the spherical primary mirror array, which relay it to the oblate ellipsoid secondary mirror, which finally focuses it onto the image focal plane. An optical trombone arrangement near the focal plane allows 2 out-of-focus images to be simultaneously recorded on two CCD arrays for phase-diversity wavefront sensing analysis. An MS Windows computer contains National Instrument devices for commanding piezo actuators that control the articulated primary mirror elements, and for controlling the data acquisition by the CCD arrays mirror assembly, which consists of a hyperboloid secondary and an off-axis paraboloid primary. The collimated light is then intercepted by the elements of the spherical primary mirror array, which relay it to the oblate ellipsoid secondary mirror, which finally focuses it onto the image focal plane.

2.1 Optical System Design

The FIT optics design is chosen to incorporate many of the essential elements of the SI instrument on a smaller scale. Specifically, the primary mirror of the imager assembly is chosen to be of spherical shape, which significantly reduces the manufacturing cost of the mirror segments since each mirror is the same. It also simplifies the external metrology system which will be used during the initial phasing of the array as well as for continuous monitoring of the optics stability. We have already available an off-axis paraboloid collimator which has a 3 meter focal length, 12 inches of optical quality aperture with a de-center distance of 200 mm. Therefore all the subsequent optics design assumes the use of this piece of existing optics. Through an optimization process of the collimator and imager optics design we found that the maximum useable aperture is limited (by aberration as well as by blockage) to approximately 10 inches. Figures 1 and 2 show the optical layout and a photograph of FIT, both of which will be described in more detail here.

Source Module: Both a HeNe laser and a broadband light source is used to illuminate a user selectable set of pinholes, calibration masks and extended scenes. Optics are used internal to the source module to ensure nearly Lambertian illumination over the acceptance solid angle of the collimator over the field of view of the system. The set of pinholes vary from 10 to 50 mm in diameter and extend from below the resolution limit to slightly larger than the resolution limit. The set will be used with various phase retrieval algorithms in the initial alignment to observe the optical point spread function (PSF) and to estimate the modulation transfer function (MTF) of the optical system. The calibration masks consist of a chirped MTF pattern, linear gradient masks and flat fielding masks on 35 mm slide film. The MTF patterns are used to determine the combined spatial transfer function of the optical system and the process of transferring extended scene digital images to the 35 mm slide film. The OTF deduced from the pinhole and the MTF deduced from the chirped MTF patterns can be used to separate the MTF's of the optical system from the transfer of the digital images to the 35 film. This is necessary to ultimately deduce the overall image quality of the system after phase diversity and deconvolution are applied, i.e. we desire to directly compare the pre- and post-

processed images against the *true* digital image to deduce the spatial frequency response of the system for extended scene imaging. The linear gradient mask and the flat fielding mask are used in the calibration of the system to deduce linearity of the detector, to deduce gain and offset, and to correct for flat fielding errors. The extended scene masks consist of a simulated image of solar disk and a Landsat-7 scene (Figure

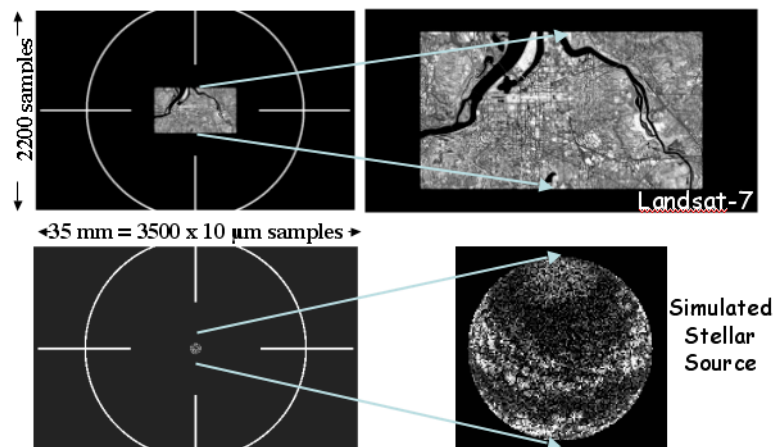


Figure 3 – FIT Extended Scenes
 Top Row: Landsat-7 Scene
 Bottom Row: Simulated Stellar Scene

processed images against the *true* digital image to deduce the spatial frequency response of the system for extended scene imaging. The linear gradient mask and the flat fielding mask are used in the calibration of the system to deduce linearity of the detector, to deduce gain and offset, and to correct for flat fielding errors. The extended scene masks consist of a simulated image of solar disk and a Landsat-7 scene (Figure

3) and are used in the final open- and closed-loop operations of the system with extended scene phase diversity. The solar disk scene represents an object which is compactly supported, i.e. the region over which the image is non-black is smaller than the field of view of the system. The Landsat-7 scene represents a non-compactly supported object which extends beyond the field of view of the system. The two types of scenes are used to test the different phase diversity algorithms (wavefront sensing) since the algorithms are significantly different for these 2 classes of objects.

Optical System: ZEMAX was used to design the optical system and this design process is described in detail in [6]; only the results are described here. Following the source module an off-axis hyperboloidal secondary mirror is used to relay the beam to the sparse array of spherical mirrors mounted on an aperture plate. Each of the spherical mirrors is mounted on 3 degree of freedom (piston/tip/tilt) piezo actuators mounted on an aperture plate; in addition the mirrors can be moved (manually) on the aperture in 1-inch increments on a rectilinear grid. The right side of Figure 1 shows a photo of the aperture plate. The beam after the spherical mirrors is collimated and impinges on the off-axis parabolic collimator mirror. Following this mirror is an off-axis elliptical mirror, which images the scenes onto the detector arrays.

The optimized design parameters of the optics are:

- *Object:* diameter 2.4mm, distance to next element 1.813 m.
- *Collimator secondary:* radius of curvature of 2.863 m, conic constant of -6.65, diameter of 84 mm, decenter of 53.5 mm, distance to the next element of 2.2 m.
- *Collimator primary:* radius of curvature of 6 m, conic of -1, (useable) diameter of 254 mm, decenter of 200 mm, distance to the next element of 2.5 m.
- *Imager primary:* radius of curvature of 4 m, (useable) diameter of 254 mm, decenter 280, distance to the next element of 1.414 m.
- *Imager secondary:* radius of curvature of 1.463 m, conic of 4.5, diameter of 110 mm, decenter of 81 mm, distance to the next element of 2.948 m.
- *Image:* diameter of 3.7 mm.

Raytrace analysis shows the optical performance from the object plane to the image plane to be diffraction-limited over the 2.4mm x 2.4 mm (or 1.2' x 1.2') field-of-view.

Image Module: The image module initially consists of a 50-50 beam splitter which splits the optical path in 2 beams of equal intensity. Each beam is imaged onto a separate Finger Lakes CCD camera, 1536 x 1024 format, 16 bit TEC cooled with 9 mm pixels. Just prior to the beam splitter a lens system can be inserted on a kinematic mount to relay an image of the pupil to the pupil-imaging camera.

2.2 Mechanical Systems Design

Stability is the paramount consideration for the FIT mechanical design. In order to accommodate the scientific goals of the testbed, the system must maintain long term sub-micron level precision for each of the optical elements. In the interest of maximizing cost and time efficiency, the current system is constructed from off the shelf parts wherever possible. The main thrust of the custom design was focused on the most sensitive elements: the primary mirror array and the hyperbolic and oblate-ellipsoidal secondary mirrors. The system is installed on a TMC 4'x16' optical table that is pneumatically vibration isolated.

The hyperbolic and oblate ellipsoidal secondary mirrors are bonded into high precision 6-axis adjustable stainless steel mounts. These mirror mounts consist of Newport 562 ULTRAlign 3-axis manual linear stages and 562F-Tilt tip-tilt stages combined with a custom made interface that allows for 30° of manual rotation about the optical axis. The system optical axis plane is set to 11.50" above the table by the parabolic collimating mirror, so the secondary mirrors are mounted on standoff blocks cut to set the secondary mirror optical axes on that plane.

The primary mirror array is mounted on a baseplate with a 14x14 Cartesian grid of mounting points on 1" centers, allowing for testing of a variety of array element configurations. This plate is attached via support brackets and a custom interface to a 3-point kinematic standoff, which can provide coarse tip-tilt and height adjustment for the entire array. Each individual mirror element is bonded onto an interface plate that is in

turn bolted to a Melles Griot 17ASM003 piezoelectric tip-tilt flexure mount, giving each element the required nanometer level precision adjustment. The Preliminary thermal and stress analyses indicated that the aluminum baseplate for the primary mirror array would be sufficiently stable. This prediction has been verified by a qualitative in situ stability analysis over a period of 20+ hours.

2.3 Data Acquisition System

The 2 CCD cameras are interfaced to the processing and control computer through a USB bus. The piezo actuators are controlled through a rack mounted (National Instruments PXI-1000) PCI bus interface consisting of a National Instruments MXI-3 8335 PCI bus extender of which a 1/2 bus card is mounted within the control computer 1/2 of the bus is mounted in the rack. A National Instruments DIO 6533 D/A controller converts the digital control signals to analog voltages which are fed to the Thorlabs power supplies for driving the piezo actuators. In the current configuration there are 7 driving power supplies, one per mirror; each controls 3 degrees of freedom for each mirror.

Two primary graphical user interfaces (GUI) have been developed in LabView, one to manually control the piezo mirror actuators, and the other for manually stepping through the control loop. The first GUI mentioned consists of a series of *sliders* displayed in the GUI for manual control of the actuators, where one slider represents one degree of freedom. This allows for ease of actuator movement and image collection. The second GUI consists of a series of buttons. The first button triggers the 2 cameras and allows for collection of 2 images, one per camera. The 2nd button calibrates the images, performing background subtraction and flat fielding on both images. The 3rd button performs the wavefront sensing, and the user can select between a set of phase retrieval and phase diversity algorithms. The 4th button decomposes the wavefront into the eigenmodes of the control system – generating the actuator commands and the 5th button applies the actuator commands. A 3rd interface will be developed for the closed-loop control.

Figure 4 shows a flowchart of the control software interfaced with devices. The *executive* is the LabView interface and controls the actuators, CCD cameras, the choice of phase diversity algorithm, control law and motion of the actuators. The pupil monitor is the pupil imaging camera and the DFS is the dispersed fringe sensor to assist in coarse pistoning of the actuators. These are manually controlled by the operator.

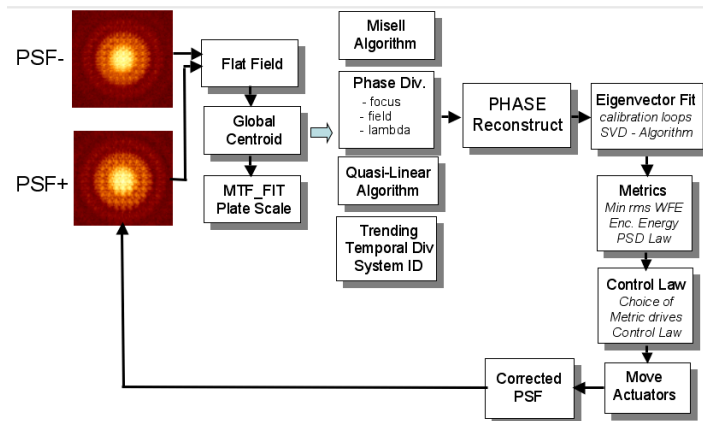


Figure 4– FIT Control Loop

Currently the source module is also controlled manually, i.e. the user must hand select which scene and set of spectral filters to use. Also the pupil imaging camera is used by manually inserting a flip mirror, on a kinematic mount, just prior to focal plane, to relay the image to the pupil imaging camera. The source module and the pupil imaging camera may be automated at a later date.

3.0 WAVEFRONT SENSING AND OPTICAL CONTROL

Multiple phase retrieval and phase diversity algorithms are used to sense the wavefront in the systems exit pupil. Phase retrieval uses an unresolved point source imaged through the optical system and relies on diffraction spreading of the point source. Phase diversity [12] uses an unknown extended scene to estimate the wavefront. The resultant wavefront is decomposed into the eigenmodes of the control system and the piezo actuators are moved to initially align to maintain alignment of the FIT system. Herein we give a brief overview, as space permits, of the wavefront sensing methods and control methods employed for FIT.

3.1 Phase Retrieval

The optical point spread function is given by:

$$PSF(x, y; \lambda, W) = \left| \iint A(u, v) e^{i \frac{2\pi}{\lambda} W(u, v)} e^{-i \frac{2\pi}{F} (xu + yv)} du dv \right|^2 \quad (1)$$

where (u, v) are the coordinates of the exit pupil and (x, y) are the coordinates in the focal plane. $A(u, v)$ represents the aperture function, i.e. region over which light passes through the pupil function; shown in Figure 5 for the initial configuration of FIT. $W(u, v)$ represents a realization of the wavefront in the exit pupil. The wavelength and system focal length are represented by λ and F respectively. Equation (1) shows that the PSF is proportional to the modulus squared of the 2D spatial Fourier transform of the complex exit pupil function. Equation (1) represents a continuous function, however, since we are using CCD arrays to collect the images some modifications are required.

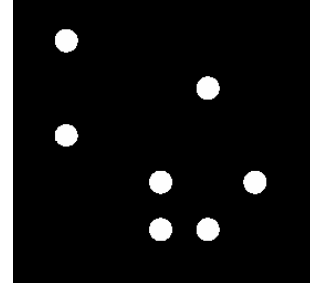


Figure 5 – FIT Aperture Function

A CCD has two primary effects (i) finite area of a pixel and (ii) sampling. Let the pixel length and widths be given by Δx and Δy respectively and let j and k represent the pixel indices in x and y running from $1 \dots N_x, N_y$. The finite pixel size can then be represented by $rect(x/\Delta x) = \{1 \text{ for } |x| \leq \Delta x/2; 0 \text{ otherwise}\}$ and the sampling can be represented by $\prod_{j=1}^{N_x} \prod_{k=1}^{N_y} \delta(x - j\Delta x) \delta(y - k\Delta y)$ where $\delta(x - j\Delta x)$ is zero for $x \neq j\Delta x$ and unity for $x = j\Delta x$. Then with no other sources of error the point response function (PRF), sampled on a discrete grid, is given by:

$$PRF(j, k; W) = \prod_{j=1}^{N_x} \prod_{k=1}^{N_y} rect\left(\frac{x}{\Delta x}\right) rect\left(\frac{y}{\Delta y}\right) \iint PSF(x, y) T(\lambda) d\lambda \prod_{j=1}^{N_x} \prod_{k=1}^{N_y} \delta(x - j\Delta x) \delta(y - k\Delta y) \quad (2)$$

where \iint represents 2D convolution and $T(\lambda)$ represents the source spectrum, spectral transmission of the optics and quantum efficiency of the detector. What is actually observed in the focal plane will also contain the effects of photon noise, readnoise and dark current noise, flat fielding errors and stray light; thus the actual observed focal plane data is represented by:

$$d(j, k; W) = flux \cdot PRF(j\Delta x, k\Delta y; W) + A \cdot j\Delta x + B \cdot k\Delta y + C + \epsilon_{jk} \quad (3)$$

Thus, succinctly stated, the phase retrieval problem is to estimate $W(u, v)$ from one or more observations of the data, i.e. $d(j\Delta x, k\Delta y; W)$. This is inherently a nonlinear problem that has been widely researched. A wide variety of optimization and *projection onto sets* algorithms exist to solve this problem. See [7][8][9] and references therein for a good overview of phase retrieval.

The *baseline* algorithm to be used is based upon a modified version of the Misell algorithm [10]. We will actually use a number of algorithms and compare the results, in terms of image quality, wavefront error, convergence and computational speed. The baseline algorithm is shown in flowchart form in Figure 6.

Baseline Algorithm

In the baseline approach 2 foci are used, i.e. the 2 FIT detectors each collect an image with a shift in their focal planes. At each focus 2 narrowband images are collected, each at a different wavelength. Thus there are 4 images in all. To start the phase retrieval a random wavefront ϕ is assumed (top of flowchart in Figure 6). The known focal shifts and wavelengths are applied, labeled as *Add Diversity* in Figure 6, and complex pupil functions are constructed. Fast Fourier Transform (FFT) techniques are used to propagate to the focal plane and the phase of this propagation is retained but the amplitude is replaced with the square root of the observed 4 images. The results are back propagated using inverse FFT techniques to reconstruct the complex pupil functions. The phase is retained and the amplitude is replaced with the amplitude of the known pupil function (aperture mask). The 4 wavefronts (phases) are mixed and an updated estimate of the wavefront is obtained. This process is iterated until a stable solution is reached. In open-loop this can take on the order of 100 iterations but in closed-loop where the temporal sampling frequency of the images is fast with respect to changes in them only a few iterations (typically 5 – 20) are required. The baseline algorithm uses both focus and wavelength diversity simultaneously for a more optimal result.

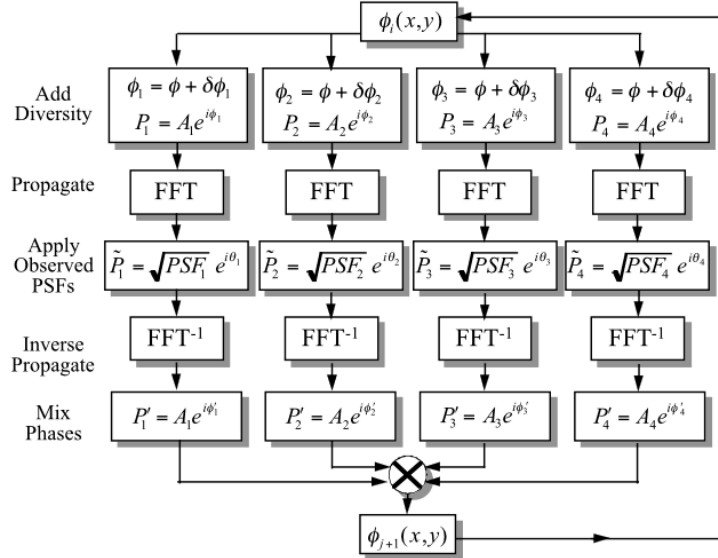


Figure 6 – Baseline Phase Retrieval Algorithm

Figure 7 shows the expected performance of the baseline wavefront sensing algorithm. The left of Figure 7 shows the expected rms wavefront error due to the algorithm, i.e. a series of 4 images, (2 foci, 2 wavelengths) with varying peak signal-to-noise (SNR) is input to the algorithm and the wavefront solved for. The rms difference between the recovered wavefront and the input is plotted. Our expected value of SNR is ~100 giving a theoretical wavefront sensing capability on FIT of ~4/1000 waves.

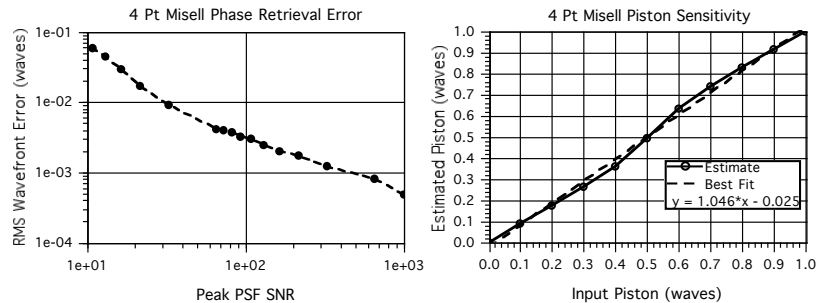


Figure 7 – Expected Performance of Phase Retrieval
 Left: Expected error in sensing of wavefront vs SNR
 Right: Estimated piston vs input piston

The rms difference between the recovered wavefront and the input is plotted. Our expected value of SNR is ~100 giving a theoretical wavefront sensing capability on FIT of ~4/1000 waves. The rightside of Figure 7 shows the error in sensing of piston only on a single mirror.

3.2 Optical Control

The wavefront sensing recovers a wavefront which is linearly related to the degrees of freedom that we can control on each of the spherical mirrors in the array. For initial configuration of FIT we can control piston, tip and tilt on the 7 mirrors, which equates to 21 degrees of freedom (DOF) in all.

For a single spherical mirror in the array we assume a linear controls model of the form:

$$\begin{bmatrix} W_1 \\ W_2 \\ \vdots \\ W_N \end{bmatrix} = \begin{bmatrix} R_{11}^{(1)} & R_{12}^{(1)} & R_{13}^{(1)} \\ R_{21}^{(1)} & R_{22}^{(1)} & R_{23}^{(1)} \\ \vdots & \vdots & \vdots \\ R_{N1}^{(1)} & R_{N2}^{(1)} & R_{N31}^{(1)} \end{bmatrix} \begin{bmatrix} A_{11}^{(1)} & A_{12}^{(1)} & A_{13}^{(1)} \\ A_{21}^{(1)} & A_{22}^{(1)} & A_{23}^{(1)} \\ \vdots & \vdots & \vdots \\ A_{31}^{(1)} & A_{32}^{(1)} & A_{33}^{(1)} \end{bmatrix} \begin{bmatrix} g_1 \\ g_2 \\ g_3 \end{bmatrix} + \begin{bmatrix} P_{01} \\ P_{02} \\ P_{03} \end{bmatrix} + \begin{bmatrix} n_1 \\ n_2 \\ n_3 \end{bmatrix} \quad (4)$$

or in a more succinct form: $\mathbf{W} = \mathbf{RAGV} + \mathbf{P}_0 + \mathbf{n}$. In the notation for equation (4) the upper index, on each matrix element, represents the mirror number and the first lower index represents the wavefront piston, tip and tilt index respectively, i.e. 1,2,3 and the 2nd lower index represents the actuator piston, tip and tilt, i.e. 1,2,3. \mathbf{W} represents the wavefront, due to that mirror, in vector format. \mathbf{R} represents the mapping of actuator piston, tip and tilt to wavefront piston, tip and tilt. This is $N \times 3$ matrix, where N is the number of wavefront sample points within a single mirror and 3 is the number of DOF per mirror. This matrix is not diagonal unity since the piezo actuators actually move the mirrors about a point not contained within the mirror surface and thus a mapping is required. \mathbf{A} represents the mapping of actuator voltages to actuator piston, tip and tilt. This is a matrix since there is redundancy in the DOF that the 3 piezo actuators per mirror can correct, i.e. moving all 3 actuators gives piston, but moving only a single actuator gives both piston and tip or tilt. \mathbf{G} is the diagonal gain matrix and represents how much gain (or damping) we desire. \mathbf{P}_0 represents a fixed offset if required and \mathbf{n} represents a vector of all noise sources on the actuators and includes, A/D, quantization, and repeatability. \mathbf{V} is the vector of actuator voltages to be solved for at each time step.

If we define the single channel (single mirror) response matrix as $\mathbf{S}^k = \mathbf{R}^k \mathbf{A}^k \mathbf{G}^k$ then the entire wavefront can be represented by:

$$\mathbf{W} = \begin{bmatrix} [\mathbf{S}^1] & [\mathbf{S}^2] & \dots & [\mathbf{S}^7] \end{bmatrix} \begin{bmatrix} V_1 \\ V_2 \\ \vdots \\ V_M \end{bmatrix} + \mathbf{n} \quad (5)$$

where $[[\mathbf{S}^1] \quad [\mathbf{S}^2] \quad \dots \quad [\mathbf{S}^7]]$ represents an augmented system of matrices, 1 per mirror and $V_{p=1..21}$ represents the voltage on each of the 21 degrees of freedom. Equation (5) can now be represented in the more compact form $\mathbf{W} = \mathbf{SV} + \mathbf{n}$ and the solution for the voltages can be converted to a constrained optimization problem of the form:

$$\square^2(\mathbf{V}) = (\mathbf{W} - \mathbf{SV})^T \mathbf{C}_n^{-1} (\mathbf{W} - \mathbf{SV}) \quad (6)$$

where $\mathbf{C}_n = \langle \mathbf{nn}^t \rangle$ is the noise covariance matrix of the wavefront sensing process. An unconstrained solution of equation (6) is given by $\mathbf{V} = (\mathbf{S}^T \mathbf{C}_n^{-1} \mathbf{S})^{-1} \mathbf{S}^T \mathbf{C}_n^{-1} \mathbf{W}$. Thus in principle we can solve for the voltages at each time step given the wavefront recovered from phase retrieval. In practice we have some additional constraints in that the voltages, and the actuators have limited range and thus we impose constraints that the mean piston over the set of mirrors is zero and also similar constraints on the tip and tilt. In addition in order to make the process more numerically efficient and stable we diagonalize the matrix $(\mathbf{S}^T \mathbf{C}_n^{-1} \mathbf{S})^{-1}$ using singular value decomposition and work only with the largest eigenmodes. This is equivalent to only moving linear combinations of actuators which give the largest gain in correction of the wavefront. For a more detailed description of this process see [11].

Note that the required matrices are incompletely known and hence contain uncertainties. For example the mapping from actuator piston, tip and tilt to wavefront piston, tip and tilt (\mathbf{R}) is based upon a mechanical model which will contain errors due to the imprecise location of the

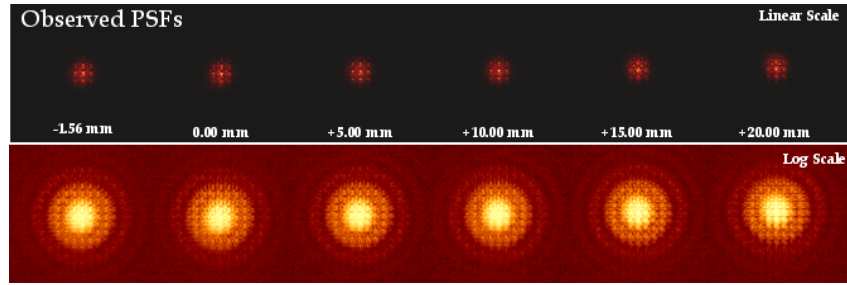


Figure 11 – Through Focus Set of PSFs

points at which the forces are applied by the piezos to the mirrors. The net effect will be to give errors in positioning of the mirrors which will tend to lower the fidelity of the controls and hence the final image quality. During the calibration phase we will explore using system identification [13] to update our initial

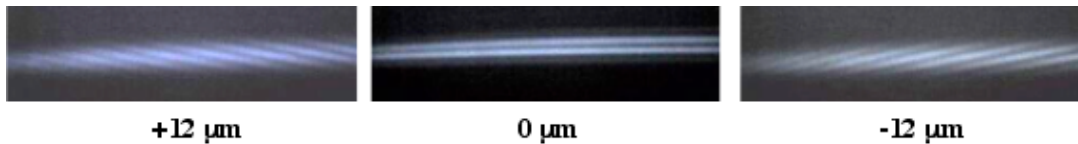


Figure 8 – FIT Dispersed Fringe Sensor Fringe Patterns

estimate of these matrices. System identification uses both the current wavefront and our predicted wavefront after correction from the previous time step, to estimate a delta wavefront which is fed back to the matrices in the control law. This technique works if the system is stable between successive time steps, or alternatively if the bandwidth is such that the sampling interval is short with respect to the time constant of any changes in the system.

4.0 PRELIMINARY RESULTS

4.1 Initial Alignment

Each of the optics in FIT has a flat bonded to its mounting structure and a master reference cube is mounted on the table. Theodolites are used to set up a coordinate system such that an optic can be removed from the system and re-inserted with minimal difficulty. A coordinate measuring machine (CMM) with approximately 10 microns of accuracy was used to coarsely align the sparse array mirror segments and to shim up the actuator mounts. A dispersed fringe sensor (DFS) was used to initially phase the mirror segments with respect to piston and to place the mirror mounts in the middle of their range. Figure 8 shows an example of the dispersed fringes from the DFS. The DFS is essentially a slitless spectrometer, where each segment mirror is imaged onto a diffraction grating and then pairwise the beams are brought to focus on a detector. Without any piston difference between the segments, a set of straight fringes results, with piston, a set of curved (barbershop pole) fringes appears as is evident in Figure 8. The

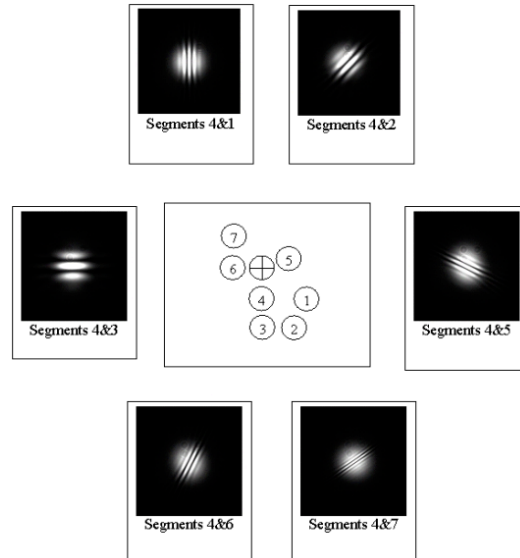


Figure 9 – FIT White Light Fringes
Pairwise white light fringe patterns

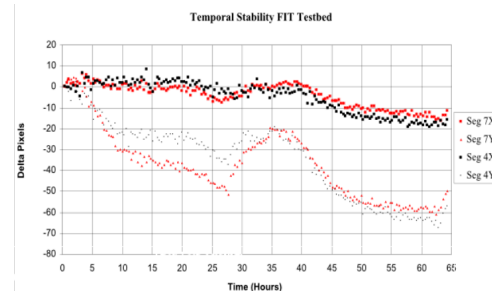


Figure 10 – Stability of FIT

DFS has large dynamic range for sensing piston (~1 mm) however its accuracy is limited at the lower end of the range and thus it can sense piston down to ~1 – 2 microns.

A series of images of a point source were also collected by imaging a point source from the center of curvature of the sparse aperture mirror array onto a detector. This effectively removed all the other optics from the system and assisted in initial piston and tip/tilt alignment of the system.

Figure 3 shows a photo of the FIT during assembly. The beam paths are drawn in green FIT is assembled on a 6 x 16 foot airtable in shrouded housing, i.e., a support structure is built around the table with a ceiling and black walls to mitigate stray light problems. Baffles are placed between the optics (not shown in Figure 3).

4.2 First Light Images

Currently we have been successful at phasing all 7 segments of FIT. Figure 9 shows examples of white light interference between aperture #4 paired against 6 of the other apertures. Figure 10 shows the stability of the fringe patterns over 65 hours with the FIT system operated in open-loop, i.e. with no correction to the actuators. Long term drifts of ~60 pixels occurred over 2 days; most of the drift coming from slowly varying thermal drift of +/- 0.7 degrees per day. The thermal drift moved the overall image on the detector, but the system still remained well phased implying that the image motion was caused by a global change in the optics mounts and not between the apertures.

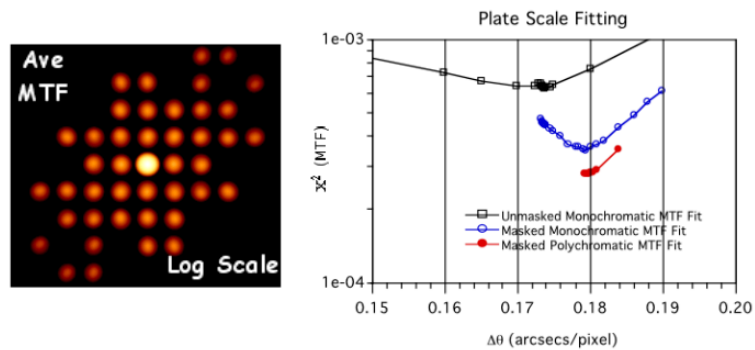


Figure 12 – FIT Plate Scale Fitting
 Left: FIT Modulation Transfer Function (UV-plane coverage)
 Right: Variance of MTF difference vs plate-scale for 3 models .

Figure 11 shows (on both a linear and log scale) a through focus sweep via translation of the focal plane. The system, being relatively slow (~F/66) gives only subtle change in the images; it is this small amount of change that the phase diversity algorithms will resolve to determine the aperture misalignments used to drive the control loop. Figure 13 shows a phase diversity result. The top-left image shows an observed image and the middle left shows the result of using the baseline algorithm to estimate the wavefront and fit it to a set of 13 full aperture Zernike polynomials, through spherical aberration, the middle right shows the residual that was not fit. The bottom left shows the results of fitting to 13 Zernike polynomials per aperture, i.e. each sub-aperture was allowed its own set; the first 3 polynomials are piston tip and tilt. It can be seen that most of the power occurs in piston tip and tilt. The lower-right again shows the residual of the fitting.

In order to perform the wavefront sensing we must have good knowledge of the FIT plate scale and/or focal length. This is determined by an optimization procedure in the MTF domain. The left side of Figure 12 shows an MTF, calculated by Fourier transforming a FIT PSF. Each of the conelike “patches” represents the a baseline pair of apertures in the spatial frequency domain. If an aperture is shifted laterally along the aperture plate then all the cones corresponding to interference of this aperture with the 6 others will also be shifted in the MTF domain. An algorithm was developed which finds the minimum, as a function of lateral shift of each aperture, of the rms difference between a simulated MTF and an MTF constructed as the Fourier transform of an observed PSF. The rightside of Figure 12 shows the minimum with 3 successively more refined models of the MTF. The top black curve of Figure 12 shows the fitting statistic versus plate scale for a monochromatic MTF model without thresholding (masking), the middle blue curve with thresholding to remove the noise between the MTF cones and the red curve using a polychromatic MTF model with thresholding. The successively more refined model both shifts the location and depth of the minimum. The net result was that each of the aperture locations was located and the plate scale was found

to be 0.1799 arcsec per 9 micron pixel yielding and effective focal length of 10.319 meters and an F/# of 66.2817.

5.0 SUMMARY AND FUTURE PLANS

Currently the Fizeau Interferometry Testbed has been designed, fabricated, assembled and aligned. Most of The source module currently only consists of a set of pinholes and spectral filters. The extended scene and calibration masks are currently being fabricated and will shortly be installed in the source module. The pupil imaging optical path is also currently under development. The LabView interface and installation of all the different phase retrieval/diversity algorithms and control software is well on the way to completion.

Following this we will begin the calibration sequence and the experiment plan to demonstrate both open- and closed-loop control of the testbed first with a point source and subsequently with extended scenes. This will initially be with the 7 mirrors in a Golay configuration but the number of mirrors will ultimately be expanded to 30 mirrors to facilitate various UV-plane samplings and their effect on system performance. We will also investigate various image deconvolution and image construction approaches, alignment methodologies, UV-plane samplings and control algorithms. Ultimately the goal of FIT is to assist in the development of requirements for the Stellar Imager mission and to identify technological readiness of the techniques required for Stellar Imager. It will also facilitate development of the error budgeting formalism for the flight mission.

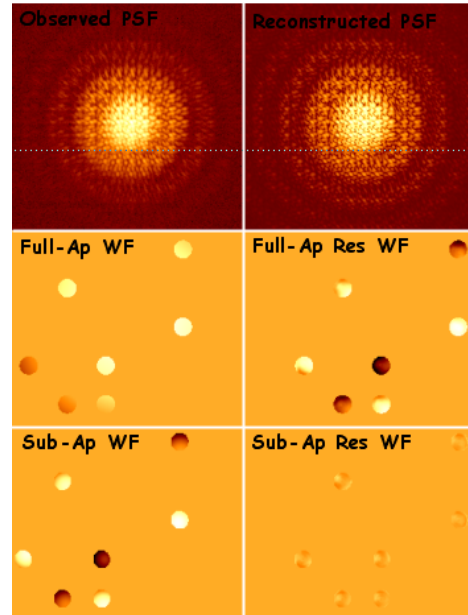


Figure 13 – FIT Phase Retrieval Results

6.0 REFERENCES

- [1] <http://hires.gsfc.nasa.gov~si>
- [2] K.G. Carpenter, C.J. Schrijver, R.G. Lyon, L.G. Mundy, R.J. Allen, J.T. Armstrong, W.C. Danchi, M. Karovska, J. Marzouk, L.M. Mazzuca, D. Mozurkewich, S. Neff, T.A. Pauls, J. Rajagopal, G. Solyar, and X. Zhang, "The Stellar Image Mission Concept," *Proc. SPIE* **4854**, 2002.
- [3] X. Zhang, L. Feinberg, D. Leisawitz, D. Leviton, A.J. Martino, and J.C. Mather, "The Wide-Field Imaging Interferometry Testbed," *Proc. IEEE Aerospace Conf.*, 2001.
- [4] M.J.E. Golay, "Point Arrays Having Compact, Nonredundant Autocorrelations," *IEEE* **61**, 272-273, 1971
- [5] S.W. Golomb, and H. Taylor, "Two-Dimensional Synchronization Patterns for Minimum Ambiguity," *IEEE Trans. Infor. Theo.* **IT-28**, No 4, 600-604, 1982
- [6] X. Zhang, K. Carpenter, R. Lyon, H. Huet, J. Marzouk, G. Solyar, "The Fizeau Interferometer Testbed", IEEE Conference, Bigsky Montana, March 2003
- [7] R.G. Lyon, J.E. Dorband, and J.M. Hollis, "Hubble Space Telescope Faint Object Camera Calculated Point-Spread Functions," *Appl. Opt.* **36**, No. 8, 1752-1765, 1997
- [8] J.R. Fienup, "Phase Retrieval Algorithms: A Comparison", *Appl. Opt.* **21**, 2758-2769, 1982
- [9] Luke, R., Burke, J.V., Lyon, R.G., *Optical Wavefront Reconstruction: Theory and Numerical Methods*, *SIAM Review*, Vol. 44, No 2 pp 169-224, May 2002
- [10] D.L. Misell, "A Method for the Solution of the Phase Problem in Electron Microscopy", *J. Phys. D* **6**, L6-L9, 1973
- [11] T.P. Murphy, R.G. Lyon, J.E. Dorband, and J.M. Hollis, "Sparse Matrix Approximation Method for an Active Optical Control System," *Appl. Opt.*, **40**, No 35, 2001
- [12] R.G. Gonsalves, "Phase Retrieval and Diversity in Adaptive Optics", *Opt. Eng.*, **21**, 829, 1982
- [13] K. Ogata, *Discrete-Time Control Systems*, Prentice-Hall Inc, Englewood Cliffs, NJ, 1987